Modal analysis of transport processes in SPRITE detectors

Frank J. Effenberger and Glenn D. Boreman

Carrier transport in signal-processing-in-the-element (SPRITE) detectors is an important phenomenon because it determines properties such as the responsivity and the modulation transfer function (MTF). The previous literature has presented approximate solutions to the transport problem that neglect boundary effects, which have long been thought to play a major role in SPRITE behavior. We present a new solution to the problem through the use of modal analysis. This method intrinsically includes boundary conditions and thus is more complete than the previous analysis. Furthermore we use this solution to derive expressions for the MTF. The effects of the boundary conditions on the MTF are studied to determine their optimum values.

Key words: SPRITE, IR detectors, charge transport, MTF.

1. Introduction

Signal-processing-in-the-element (SPRITE) detectors[1,2] provide improvement in the signal-to-noise ratio over simpler photoconductive detectors through the use of a virtual time-delay-and-integration process internal to the detector element. The drift transport of carriers through the detector is the mechanism that makes this possible. Other transport mechanisms, such as recombination and diffusion, tend to degrade detector performance. Understanding the interplay of these effects with the electrical boundary conditions would permit better understanding of existing devices and provide further guidance in the design and manufacture of new SPRITE detectors.

In previous analyses,[3–5] a one-dimensional Green's function was taken as the solution to the transport equation. This solution, which describes the charge distribution in an infinite one-dimensional solid resulting from a point source, is used as the basis of calculations to compute the transfer of a scanned incident-radiation distribution on the SPRITE detector bar into the output as seen at the readout terminals.

The authors are with the Center for Research and Education in Optics and Lasers, Department of Electrical and Computer Engineering, University of Central Florida, Orlando, Florida 32816.

Received 5 October 1994; revised manuscript received 31 January 1995.

0003-6935/95/224651-11$06.00/0.

This theory does not show complete agreement with the measurements of real devices.[6] The definition of the Green's function implicit to the analysis omits key physical phenomena in its development. The steps subsequent to the generation of the Green's function are straightforward applications of linear-systems theory and are generally valid for this type of analysis. We have therefore used a different method, modal analysis, to solve the charge-transport equation and developed an equivalent analysis of the transfer function of SPRITE detectors.

The method of modal analysis is more capable and requires fewer assumptions than the previous Green's-function method. The first improvement is that modal analysis is multidimensional, whereas the Green's-function method is one dimensional. Although the single-dimensional approach may suffice for long, slender detector bars, most practical devices have aspect ratios that are only near 10. This fact requires consideration of the transverse dimensions.

The second improvement is that the boundary conditions are included in modal analysis. The Green's function method has no boundary conditions because of the implicit assumption of an infinite solid. The boundary conditions are important because (1) the readout is usually placed at one end of the detector and (2) most contacts made to HgCdTe show partial blocking behavior,[7] which leads to carrier accumulation at the contacts. Thus the inclusion of boundary conditions has a considerable effect.

Our modal solution is found by use of the method of separation of variables on the transport equation

followed by determination of the eigenmodes of the separated equations.[8] This process is shown to include the pertinent features of the system while still producing closed-form solutions. In Section 2 a more complete definition of the SPRITE transport problem is given. Then the modal solutions are developed and described. After this, we use the modal solutions to compute the impulse response, and then this is converted into the MTF of the detector. Finally, some conclusions are drawn about the general behavior of the MTF and the modal parameters.

2. Transport Problem

SPRITE detectors are complex devices with many features that are not easily analyzed. Among these are details of the readout geometry, the electrical properties of the passivated surfaces, and the current-voltage characteristics of the electrical contacts. Although a complete model of all these factors requires a numerical solution,[9] simplifications can be made to yield a self-consistent model that can be solved analytically and yet still contains the main features. In this section such a mathematical description of the SPRITE transport problem is given.

A diagram of our idealized detector is shown in Fig. 1. The detector is a rectangular solid with length, width, and depth denoted $2l$, $2w$, and $2d$, respectively. The device has contacts on the two ends that are nominally ohmic. The top, bottom, and side surfaces are all passivated insulating boundaries. A sensing lead is placed on the bar near the output end. This lead measures the voltage across the readout zone of the detector and is connected to a high-impedance amplifier.

Operation of this detector hinges on the ambipolar drift of photon-generated minority carriers. Most HgCdTe-based SPRITE's are made of an *n*-type semiconductor, and thus the minority holes carry the signal of interest. If the light source is scanned along the length of the bar, and the carriers drift along with it at the same speed, the detected signal is amplified and reinforced. This process shows the same character and advantages as a time-delay-and-integration system but without the necessity of separate delay-line electronics. When the intensified charge reaches the end of the detector, it causes the voltage on the sensing lead to change, thus generating a signal.

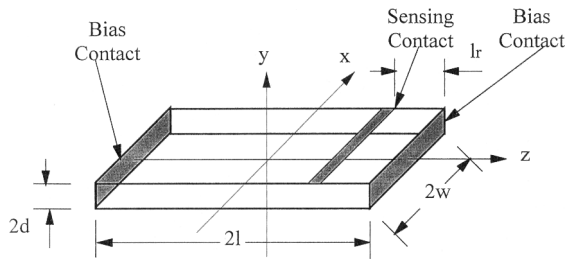

Fig. 1. SPRITE detector model geometry and coordinate system.

The basis for the model is the transport equation:

$$\frac{\partial \rho}{\partial t} = D\nabla^2\rho - \mu\nabla \cdot (\rho E_z \hat{k}) - \frac{\rho}{\tau} + G. \tag{1}$$

This equation assumes that the carriers in the device can be described by a volumetric density ρ, and the material can be described by a diffusivity D, mobility μ, and minority carrier lifetime τ and that there is a spatially invariant generation rate G. These assumptions ignore the particulate nature of the charge and the resultant inherent randomness of their generation, motion, and recombination. Thus it can be said that this equation deals with the average values for all the quantities concerned and is deterministic. This equation also neglects the momentum of the carriers, assuming that the mean free path in the material is short compared with any other dimension of the device. This last assumption is valid in SPRITE structures because the devices are long and the electric fields are low.

The major assumption implicit in Eq. (1) is that the product of the electric field and mobility, which equals the carrier-drift velocity, is assumed to be constant. This implies that the device is designed and operated in a manner that generates this condition at steady state. For simple rectangular detectors, integration of the background radiation causes this product to vary slowly over the length of the bar, with a total change of $\sim$25%.[9] By tapering the detector bar, this nonuniformity can be reduced to insure a constant drift velocity. Also Eq. (1) assumes that the photogenerated carriers themselves do not generate significant space-charge fields. This is true for SPRITE's because the bias current and its associated electric bias field are much stronger than the detected image signal and its field.

The boundaries of the bar, as mentioned above, are nominally either ohmic or insulating. Observations on actual devices,[10] however, indicate behavior that differs from ideal conduction or insulation. Although real surfaces are difficult to describe fully, we take the first level of complexity, which is to ascribe a surface velocity V_s to the passivated surfaces and to the contacts.[11] The surface velocity relates the carrier density at the surface to the carrier flux, leaving through that surface according to

$$\mathbf{\Phi} \cdot \hat{n} = V_s\rho. \tag{2}$$

Carrier flux $\mathbf{\Phi}$ is a vector quantity, and the normal unit vector $\hat{n}$ is defined to be pointing out of the detector volume. The flux is caused by diffusion and drift in our model and thus can be written as

$$\mathbf{\Phi} = -D\nabla\rho + \mu E_Z\rho. \tag{3}$$

If we apply this definition to the six surfaces of the detector bar, using the coordinate system shown in Fig. 1, we can produce three pairs of equations that

describe the boundary conditions:

$$D\frac{\partial \rho}{\partial x} = V_x \rho|_{x=-w}, \quad D\frac{\partial \rho}{\partial x} = -V_x \rho|_{x=+w}, \tag{4a}$$

$$D\frac{\partial \rho}{\partial y} = V_y \rho|_{y=-d}, \quad D\frac{\partial \rho}{\partial y} = -V_y \rho|_{y=+d}, \tag{4b}$$

$$D\frac{\partial \rho}{\partial z} = (\mu E + V_z)\rho|_{z=-l}, \quad D\frac{\partial \rho}{\partial z} = (\mu E - V_z)\rho|_{z=l}. \tag{4c}$$

Note that Eqs. (4) assume that the bias contacts are formed exclusively on the endfaces of the detector bar, neglecting any geometrical details of the actual contacts. Real contacts are typically formed partly on the endface and partly on the top face. Such a contact dictates boundary-condition equations that cannot be easily incorporated into our solution. Our idealized bias-contact geometry is a close approximation to reality when the top contact length is small compared with the thickness of the detector bar. Also, Eqs. (4) ignore any effects of the sensing contact. This is a good approximation if this contact is made small and if the amplifier used has a sufficiently high impedance.

The transport equation and the three pairs of boundary conditions fully describe our SPRITE-transport model. This model does not ignore any feature of the detector that is vital to its operation. As shown in Section 3, it also has a closed-form solution. These factors result in a model that is more realistic than other models described previously.

3. Modal Solutions

The first step in the solution of Eq. (1) is to perform a transformation of the dependent variable to make the equation homogeneous. This discards that part of the charge distribution, equal to $G\tau$, caused by background illumination. As mentioned above, the background charge influences detector performance in a deleterious way by making the drift velocity vary over the length; however, in all the following calculations it is assumed that steps have been taken to correct for this problem and the effect is ignored. Regardless of its spatial distribution, the background charge is constant in time. It therefore represents an unchanging offset on the signal and is of no interest as far as signal transfer is concerned. The transformation is

$$\rho = \rho' + G\tau. \tag{5}$$

Next, we scale all the independent variables to the natural metrics of the problem, namely, the detector dimensions for the spatial coordinates and the carrier lifetime for the time:

$$x' = \frac{x}{w}, \qquad y' = \frac{y}{d}, \qquad z' = \frac{z}{l}, \qquad t' = \frac{t}{\tau}. \tag{6}$$

The scaled coordinates are all denoted by a prime, which results in the following equation (with vector operators expanded):

$$\frac{\partial \rho'}{\partial t'} = \tau D\left(\frac{\partial^2 \rho'}{w^2 \partial x'^2} + \frac{\partial^2 \rho'}{d^2 \partial y'^2} + \frac{\partial^2 \rho'}{l^2 \partial z'^2}\right) - \frac{\mu E_z \tau}{l}\frac{\partial \rho'}{\partial z'} - \rho'. \tag{7}$$

Next we employ the technique of separation of variables, which assumes that the solution for ρ' can be written as

$$\rho' = T(t')X(x')Y(y')Z(z')\exp\left(\frac{\mu E_z l}{2D}z'\right). \tag{8}$$

This generates one time equation and three space equations:

$$\frac{\partial T}{\partial t'} + k^2 T = 0, \tag{9a}$$

$$\frac{\partial^2 X}{\partial x'^2} + k_x^2 X = 0, \tag{9b}$$

$$\frac{\partial^2 Y}{\partial y'^2} + k_y^2 Y = 0, \tag{9c}$$

$$\frac{\partial^2 Z}{\partial z'^2} + k_z^2 Z = 0. \tag{9d}$$

We have defined the time separation constant to be k^2 and the x, y, and z separation constants to be k_x^2, k_y^2, and k_z^2, respectively. These constants are related by the simple equation

$$k^2 = N_{sx}k_x^2 + N_{sy}k_y^2 + N_{sz}k_{zr}^2 + N_{dz}^2 N_{sz} + 1. \tag{10}$$

We have defined the dimensionless combinations of constants in Eq. (10) as follows:

$$N_{sx} = \frac{D\tau}{w^2}, \quad N_{sy} = \frac{D\tau}{d^2}, \quad N_{sz} = \frac{D\tau}{l^2}, \quad N_{dz} = \frac{\mu E_z l}{2D}. \tag{11}$$

The constants denoted N_{sx}, N_{sy}, N_{sz} are the ratios of the carrier recombination lifetime to the carrier spatial-relaxation lifetimes, and they depend on the physical dimensions of the detector, the diffusivity, and the carrier lifetime of the material. By the spatial-relaxation lifetime, we refer to the characteristic time for localized disturbances in the carrier distribution to spread because of diffusion. The magnitude of N_{sx}, N_{sy}, N_{sz} determines whether diffusion or recombination is the dominant process of carrier-distribution relaxation. The constant N_{dz} relates the lifetime of the charge distributions to the transit time of carriers in the device. It determines the degree of diffusional spreading that occurs during the time the carriers drift and accumulate in the detector.

We note that the time equation is of first order and has the solution

$$T(t') = \exp(-k^2 t'). \tag{12}$$

The x, y, and z equations are second order and have general solutions:

$$X(x') = c_{xp}\cos\left(k_{xp}x' + p\frac{\pi}{2}\right), \tag{13a}$$

$$Y(y') = c_{yq}\cos\left(k_{yq}y' + q\frac{\pi}{2}\right), \tag{13b}$$

$$Z(z') = c_{zr}\cos\left(k_{zr}z' + r\frac{\pi}{2}\right), \tag{13c}$$

where p, q, and r are the serial numbers for the x, y, and z solutions, respectively.

Now that the general solutions have been written, the boundary conditions can be applied. Because the variables have been scaled and separated, Eqs. (4) must be modified, producing new equations:

$$\frac{\partial X}{\partial x'} = N_{bx}X\big|_{x'=-1}, \qquad \frac{\partial X}{\partial x'} = -N_{bx}X\big|_{x'=+1}, \tag{14a}$$

$$\frac{\partial Y}{\partial y'} = N_{by}Y\big|_{y'=-1}, \qquad \frac{\partial Y}{\partial y'} = -N_{by}Y\big|_{y'=+1}, \tag{14b}$$

$$\frac{\partial Z}{\partial z'} = N_{bz}Z\big|_{z'=-1}, \qquad \frac{\partial Z}{\partial z'} = -N_{bz}Z\big|_{z'=+1}, \tag{14c}$$

where we define three new dimensionless boundary numbers:

$$N_{bx} = \frac{V_x w}{D}, \qquad N_{by} = \frac{V_y d}{D}, \qquad N_{bz} = \frac{V_z l}{D}\cdot \tag{15}$$

These constants describe the ratio of the boundary velocities with the diffusion velocity, that is, the velocity at which diffusion spreads disturbances across the device. It provides a comparison of the speed of surface recomination with the speed of diffusion.

By substituting the general solutions into these equations, we can find the allowed values of the separation constants, thus completing the solution. This results in the following transcendental relations:

$$k_{xp} = N_{bx}\cot\left(k_{xp} + p\frac{\pi}{2}\right), \tag{16a}$$

$$k_{yq} = N_{by}\cot\left(k_{yq} + q\frac{\pi}{2}\right), \tag{16b}$$

$$k_{zr} = N_{bz}\cot\left(k_{zr} + r\frac{\pi}{2}\right)\cdot \tag{16c}$$

Figure 2 is a graph of the first few roots of any of Eqs. (16) as a function of the boundary parameter, N_{bx}, N_{by}, or N_{bz}. A series of roots results from this type of equation because the mode indices, p, q, or r, can assume all positive integer values. For small or large values of the boundary parameter, the curves tend toward limiting asymptotes.

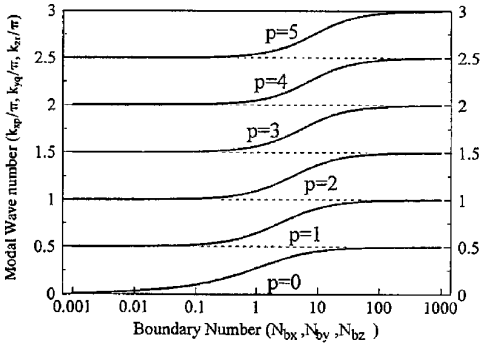

Fig. 2. Solutions to the modal wave numbers versus boundary number. Note how the solutions approach the asymptotes.

So far we have named seven independent dimensionless numbers that describe the model of the SPRITE detector. We now show that this is the correct number of constants needed to describe the problem as given. The model developed in Section 2 has nine independent parameters: length, width, and depth of the detector; surface velocities of the ends, sides, and faces; diffusivity; lifetime; and drift velocity. With this problem two units of measure are used, length and time. The π theorem[12] states that the number of independent dimensionless constants needed to describe a problem is equal to the number of measured parameters less the number of units of measure. Thus for our problem this states that seven numbers are necessary. Because the seven numbers defined here are independent from one another, they must form a sufficient, complete set of numbers completely describing the problem. To provide a feeling for the usual ranges for these numbers, typical values for these numbers have been computed with the data in Refs. 2 and 7 and are shown in Table 1.

Although our set of dimensionless numbers are complete, they do not represent the only set of numbers that could be formulated that have this property. What makes them particularly useful for our analysis is that they appear so naturally and explicitly in the differential equations and their solutions. This both eases the expression of the solutions and provides insight into the actual influence of the device parameters on device performance. This can be seen in the case of the boundary numbers.

Intuitively the best detector will have no recombination on the sides and faces and have ohmic contacts at the ends. Any realistic fabrication process cannot

Table 1. Typical Values of the Detector Numbers for SPRITE Detectors

Parameter	Value
N_{dz}	75
N_{bx}	15×10^{-3}
N_{by}	2.5×10^{-3}
N_{bz}	3.75
N_{sx}	1.0
N_{sy}	36
N_{sz}	6.4×10^{-3}

achieve such surfaces, however, and thus the question is raised as to how good the surfaces need to be. This question can be answered through use of the boundary numbers. The asymptotic behavior shown in Fig. 2 demonstrates that, for sufficiently large or small values of the boundary number, no further change in the modal wave numbers occurs. Because these wave numbers are the only way in which the boundary conditions can affect the final solution, we can justifiably say that, for practical purposes, a boundary number of less than $1/100$ is insulating and that a boundary number greater than 100 is ohmic.

The equations above describe the complete family of solutions to the transport problem. Their application requires finding the roots of Eqs. (13), which are transcendental. This makes their use difficult. It is thus interesting to look at the idealized case where the contacts are purely ohmic ($N_{bz} = \infty$) and the insulating surfaces are truly blocking ($N_{bx} = N_{by} = 0$). This results in a simple set of solutions for k_{xp}, k_{yq}, k_{zr}.

$$k_{xp} = p\,\frac{\pi}{2}, \qquad k_{yq} = q\,\frac{\pi}{2}, \qquad k_{zr} = (r+1)\,\frac{\pi}{2}. \tag{17}$$

These ideal boundary conditions enable us to write the full solution for ρ' as

$$\rho'(x', y', z', t') = \sum_{p,q,r} c_{pqr} \exp(-k_{pqr}{}^2 t') \cos\left[p\,\frac{\pi}{2}(x'+1)\right] \times \cos\left[q\,\frac{\pi}{2}(y'+1)\right] \sin\left[r\,\frac{\pi}{2}(z'+1)\right], \tag{18a}$$

$$k_{pqr}{}^2 = \frac{\pi^2}{4}(N_{sx}p^2 + N_{sy}q^2 + N_{sz}r^2) + N_{sz}N_{dz}{}^2 + 1. \tag{18b}$$

In Section 4 we show that the assumption of these boundary conditions greatly simplifies the computational form of the transfer function.

4. Modulation Transfer Function

Now that the behavior of the individual modes of the SPRITE structure have been determined, we can derive the modulation transfer function (MTF) of the detector. The MTF provides the most convenient expression of signal fidelity performance for imaging systems. Thus it is useful to compute the MTF from the physical parameters of the device. In this section we derive a general form for the MTF and special cases that result in simplification. Several families of MTF curves are computed and compared to detect trends in the general character of the MTF as a function of detector parameters.

We first define the input presented to the detector. Because the SPRITE is used as a one-dimensional detector, we use a one-dimensional δ function that can be scanned across the detector aperture:

$$q_i(z', t') = \delta(z' - z_0'), \tag{19}$$

where the scanned location z_0' is given by

$$z_0' = v't' = t'/\bar{v}'. \tag{20}$$

The constants in Eq. (20), v' and $\bar{v}'$, represent the normalized scanning velocity and its inverse, respectively. Because the scan is typically matched to the drift velocity, we can write

$$v' = \frac{\tau}{l}\,\mu E_z = 2\left(\frac{\mu E_z l}{2D}\right)\left(\frac{D\tau}{l^2}\right) = 2N_{dz}N_{sz}. \tag{21}$$

Although this input is one-dimensional, the three-dimensional nature of our solution does not necessarily vanish. When decomposed, this input produces a three-dimensional series of modes, each with its own decay-time constant. We now decompose this input into the modes of the structure:

$$q_i = \sum_{p,q,r} c_{pqr} X_p(x') Y_q(y') Z_r(z') \exp(N_{dz}z'). \tag{22}$$

Because the circular-function portion of the eigenfunctions are orthogonal, we can solve for the amplitudes of the individual modes arising from the input at any particular point z_0', giving

$$c_{pqr} = \frac{\iiint \mathrm{d}x'\mathrm{d}y'\mathrm{d}z' X_p(x') Y_q(y') Z_r(z') \exp(-N_{dz}z') \delta(z' - z_0')}{\iiint \mathrm{d}x'\mathrm{d}y\mathrm{d}z' X_p{}^2(x') Y_q{}^2(y') Z_r{}^2(z')}, \tag{23}$$

Performing the indicated integrations over the entire domain of the detector, $-1 < x' < 1$, $-1 < y' < 1$, $-1 < z' < 1$, we obtain

$$c_{pqr} = \frac{|\mathrm{sinc}(k_{xp})|}{[1 + |\mathrm{sinc}(2k_{xp})|]} \frac{|\mathrm{sinc}(k_{yq})|}{[1 + |\mathrm{sinc}(2k_{yq})|]} \times \frac{\exp(-N_{dz}z_0')\cos\left(k_{zr}z_0' + r\,\frac{\pi}{2}\right)}{[1 + |\mathrm{sinc}(2k_{zr})|]} \tag{24}$$

if p and q are even. If p or q is odd, $c_{pqr} = 0$. These mode coefficients represent the amplitude of each

mode that results from the δ-function input at the specified z' coordinate z_0'. These amplitudes then fully specify the carrier distribution inside the detector for all time after the input. Thus these mode coefficients essentially translate the given input into a charge distribution inside the detector.

We next evaluate the output voltage resulting from a given set of modes as they decay over time. In the SPRITE the measured output voltage is proportional to the charge in the readout region. The output resulting from charge generation located at z_0' is thus proportional to the charge in the readout volume Q given by

$$Q(t', z_0') = \sum_{pqr} c_{pqr} u(t' - \bar{\nu}' z_0') \times \exp[-k_{pqr}^2 (t' - \bar{\nu}' z')] b_{pqr}, \quad (25)$$

where b_{pqr} are the mode output weighting factors, given by the integration of the eigenfunctions over the scaled readout volume:

$$b_{pqr} = \int_{-1}^{1} dx' \int_{-1}^{1} dy' \int_{1-l_{r'}}^{1} dz' X_p(x') Y_q(y') Z_r(z') \times \exp(-N_{dz} z'). \quad (26)$$

Evaluation of these integrals give the result

$$b_{pqr} = \frac{|\mathrm{sinc}(k_{xp})|\,|\mathrm{sinc}(k_{yq})|}{N_{dz}^2 + k_{zr}^2} \exp(N_{dz}) \left\{ \begin{aligned} &[1 - \cos(k_{zr} l_r')]\left[N_{dz} \cos\left(k_{zr} + r\frac{\pi}{2}\right) + k_{zr} \sin\left(k_{zr} + r\frac{\pi}{2}\right)\right] \\ &+ \sin(k_{zr} l_r')\left[N_{dz} \sin\left(k_{zr} + r\frac{\pi}{2}\right) + k_{zr} \cos\left(k_{zr} + r\frac{\pi}{2}\right)\right] \end{aligned} \right\}, \quad (27)$$

if p and q are even. If p or q is odd, $b_{pqr} = 0$.

The total scanned impulse response Θ as a function of time is the point impulse response Q integrated over the entire scan, that is, over the entire detector.

$$\Theta(t') = \int_{-1}^{1} dz_0' Q(t', z_0'). \quad (28)$$

Because we are ultimately interested in obtaining the transform of the scanned function $\bar{\Theta}$, we choose to take the transform now, yielding

$$\bar{\Theta}(\omega') = \int_{-1}^{1} dz_0' \bar{Q}(\omega, z_0'). \quad (29)$$

We thus need the time-domain Fourier transform of $Q(t, z)$, which can be found to be

$$\bar{Q}(\omega', z_0') = \mathcal{F}\{Q(t', z_0')\} = \sum_{pqr} c_{pqr} b_{pqr} \frac{\exp(-j\bar{\nu}'\omega' z_0')}{k_{pqr}^2 + j\omega'}. \quad (30)$$

Substituting this into the integral for the total output, we can write

$$\bar{\Theta}(\omega') = \int_{-1}^{1} dz_0' \sum_{pqr} c_{pqr}' \frac{\exp(-N_{dz} - j\bar{\nu}'\omega') z_0'}{k_{pqr}^2 + j\omega'} \times \cos\left(k_{zr} z_0' + r\frac{\pi}{2}\right), \quad (31)$$

where we have defined a new set of constants c_{pqr}', which contains all the factors independent of the position of the input z_0'. We do this because we must integrate over this variable, and these factors will not play a role in this integration. These constants are defined as

$$c_{pqr}' = b_{pqr} \frac{|\mathrm{sinc}(k_{xp})||\mathrm{sinc}(k_{yq})|}{[1 + |\mathrm{sinc}(2k_{xp})|][1 + |\mathrm{sinc}(2k_{yq})|][1 + |\mathrm{sinc}(2k_{zr})|]}, \quad (32)$$

If we now integrate Eq. (31) term by term, we arrive at the final result:

$$\bar{\Theta}(\omega') = \sum_{pqr} \frac{c_{pqr}' \left\{ \begin{aligned} &[\exp(-N_{dz} - j\bar{\nu}'\omega' z') + (-1)^r \exp(N_{dz} + j\bar{\nu}'\omega' z')] \\ &\times \left[k_{zr} \sin\left(k_{zr} + r\frac{\pi}{2}\right) - (N_{dz} + j\bar{\nu}'\omega') \cos\left(k_{zr} + r\frac{\pi}{2}\right)\right] \end{aligned} \right\}}{[k_{pqr}^2 + j\omega'][(N_{dz} + j\bar{\nu}'\omega')^2 + k_{zr}^2]}. \quad (33)$$

Thus

This is an expression for the Fourier transform of the impulse response of a SPRITE detector as described by our model. The MTF is simply the normalized magnitude of this function, writ-

ten as

$$\mathrm{MTF}(f_z) = \left| \frac{\bar{\Theta}(2\pi l \nu' f_z)}{\bar{\Theta}(0)} \right|, \tag{34}$$

where f_z is the spatial frequency measured in cycles per unit length (i.e., cycles/mm). Note that in the figures cited in Section 5, the frequency is given in terms of cycles per detector length.

This transfer function is admittedly complex, but one can observe a few general facts about its structure. It is an infinite sum of terms, each composed of three factors. The first factor $c_{pqr}{}'$ is a modal weight that depends on the particular parameters of the structure. These weights decrease in size with increasing modal serial numbers, which ensures a bounded response. The second, the denominator in Eq. (33), is a combination of complex poles that describes the main low-pass filtering of the device. The characteristic frequency of these poles increases with the modal serial numbers. The third, which is the factor of Eq. (33) enclosed in braces, is a phasing factor that describes the coherence of the signal integration over the length of the device, which depends on the scanning velocity. These three properties all contribute to the proper functioning of the SPRITE detector.

If the boundary parameters are either very small (less than 0.01) or very large (greater than 100), as mentioned above, considerable simplification can result. We demonstrate this by two steps: first, by making the walls of the device perfect insulators and, second, by adding the constraint that the contacts are perfectly ohmic.

When the walls are perfect insulators, their recombination velocity is zero; thus the x and y boundary numbers are also zero. This greatly simplifies the modal weights, and all elements where p or q is nonzero vanish. The remaining modal weights can be written as

$$c_{pqr}{}' = \frac{\exp(N_{dz})}{({N_{dz}}^2 + {k_{zr}}^2)[4 + 4|\mathrm{sinc}(2k_{zr})|]} \left\{ \begin{array}{l} [1 - \cos(k_{zr} l_r')]\left[N_{dz} \cos\left(k_{zr} + r\frac{\pi}{2}\right) + k_{zr} \sin\left(k_{zr} + r\frac{\pi}{2}\right)\right] \\ \quad + \sin(k_{zr} l_r')\left[N_{dz} \sin\left(k_{zr} + r\frac{\pi}{2}\right) + k_{zr} \cos\left(k_{zr} + r\frac{\pi}{2}\right)\right] \end{array} \right\} \tag{35}$$

if $p = q = 0$; $c_{pqr}{}' = 0$ otherwise.

This simplification collapses the three-dimensional sum of Eq. (33) into a one-dimensional sum over the integer values of r alone and yields considerable savings in numerical effort in the calculation of the MTF.

When the contacts are made completely ohmic, in addition, all three factors in the terms of the transfer function are affected. The modal weights can then be written

$$c_{00r}{}' = \frac{(-1)^r \exp(N_{dz})}{4\left[{N_{dz}}^2 + \left(\frac{\pi}{2}\right)^2 (r+1)^2\right]} \times \left\{ \begin{array}{l} \left\{1 - \cos\left[\left(\frac{\pi}{2}\right)(r+1) l_r'\right]\right\}\left(\frac{\pi}{2}\right)(r+1) \\ \quad + N_{dz} \sin\left[\left(\frac{\pi}{2}\right)(r+1) l_r'\right] \end{array} \right\}, \tag{36}$$

and the total output spectrum can be written

$$\Theta(\omega') = \sum_r c_{00r}{}' \frac{[(-1)^r \exp[-(N_{dz} + j\bar{\nu}'\omega')] + \exp(N_{dz} + j\bar{\nu}'\omega')]\frac{\pi}{2}(r+1)}{\left\{N_{sz}\left[{N_{dz}}^2 + \left(\frac{\pi}{2}\right)^2 (r+1)^2\right] + 1 + j\omega\right\}\left[(N_{dz} + j\nu'\omega')^2 + \left(\frac{\pi}{2}\right)^2 (r+1)^2\right]}. \tag{37}$$

At this point the solution does not involve transcendental roots which enables us to write the solution in a closed form.

The finite extent of the readout area was intrinsic to the development of the results here. To remove the filtering effects caused by the spatial convolution of the readout with the image,[13] we can take the limit of the result as the readout length approaches zero. This changes only the modal weights, generating

$$c_{00r}{}' = \frac{(-1)^r \exp(N_{dz}) N_{dz}\left(\frac{\pi}{2}\right)(r+1) l_r'}{4\left[{N_{dz}}^2 + \left(\frac{\pi}{2}\right)^2 (r+1)^2\right]}. \tag{38}$$

These modal weights can then be substituted back into the transfer function [Eq. (37)].

Because the MTF is expressed as an infinite sum, we can compute only an approximation of its value. This inaccuracy is in the computation only and can be arbitrarily reduced through the inclusion of more

terms in the series and by the use of higher-precision computation. It is important to determine the number of terms necessary to achieve a given level of accuracy. The x and y summations are driven to converge by the sinc^2 functional dependence of the modal weights. Our studies show that, for the typical values listed above, the x and y series converge to 0.1% in very few terms (of the order of 10). The z-series behavior can be understood best by observing the simplified case of perfect boundary conditions. The sum, whose terms alternate sign, is driven to convergence by the factors $N_{dz}^2 + (\pi/2)^2(r + 1)^2$ in the denominator of each term. Thus it is necessary to continue the sum until the z serial number is much larger than the drift number N_{dz}. We find that of the order of 10,000 terms are necessary to achieve 0.1% accuracy.

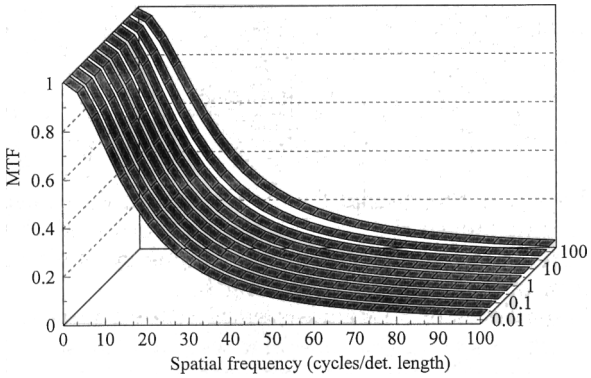

Fig. 4. MTF versus the frequency as top, bottom, and side boundary parameters are varied from 0.01 to 100 times the normal value.

5. Results and Discussion

A computer program was developed to evaluate Eq. (33) for a given set of parameters and frequencies. We used a Microsoft FORTRAN compiler running on a 486DX2/66-based desktop personal computer. Double-precision computations were used to preserve the accuracy of the sum because the sum's oscillatory behavior tends to amplify round-off errors. MTF curves could be generated in less than 10 min with this system, thus proving the tractability of this numerical approach.

Figure 3 shows the MTF for a detector with the typical values given in Table 1 along with the curve as computed with the Green's-function analysis for the same parameters in Refs. 3–5. Both show similar low-pass behavior, but the modal analysis predicts a lower roll-off frequency than the Green's-function analysis. This would put the modal analysis in better agreement with the measured responses of real SPRITE devices.

Because the modal analysis includes the boundary conditions in the solution of the problem, we can study their effects. In Fig. 4 we have plotted MTF's of detectors with different insulating surface-recombination rates. The velocity was varied from 1/100 to 100 times the nominal value in Table 1. The resultant curves show little or no effect on the MTF until the surface recombination becomes fairly strong. It is interesting that the less insulating the sides become, the wider the MTF's become. This can be understood by considering the surface recombination as a modal-damping effect. Higher recombination makes the higher transverse modes of the device dissipate faster, and this makes the overall response faster. However, dissipation of the signal charge also reduces the absolute signal levels. This can be seen in Fig. 5, which shows the signal transfer function (SiTF) for the same conditions as in Fig. 4. The SiTF shown is obtained by normalizing all the curves by the zero-frequency response of the typical parameter response. From this figure it is clear that the broadening of the MTF comes at the cost of a reduction in the level of the signal at all frequencies. Figure 6 shows the zero-frequency SiTF plotted as a function of the insulating boundary condition. The signal level is normalized to one at the nominal value of insulating boundary parameters, and it drops as these parameters are made more conductive. We can thus conclude that it is best to reduce the surface recombination, but only because it improves the signal efficiency of the detector and not because of MTF considerations.

The effect of the width of the SPRITE detector can be studied directly with modal analysis. It was

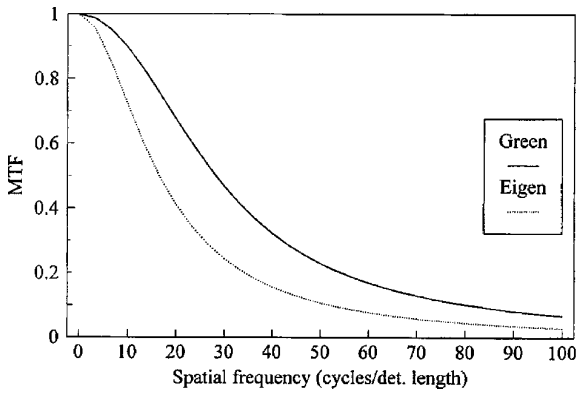

Fig. 3. Computed MTF's for the Green's-function method and the eigenmode method.

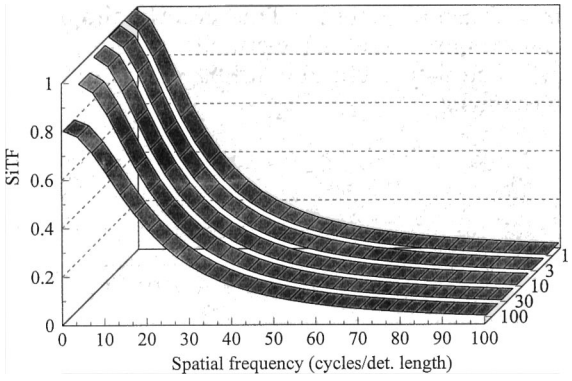

Fig. 5. SiTF versus the frequency as top, bottom, and side boundary parameters are varied from 1 to 100 times the normal value.

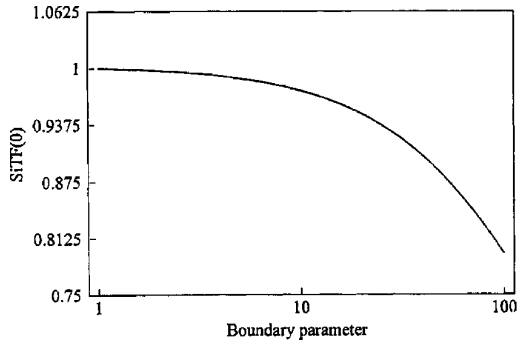

Fig. 6. Variation of the zero-frequency SiTF as top, bottom, and side boundary parameters are varied from 1 to 100 times the normal value.

found that, with the top, bottom,, and side boundary parameters set to their normal values, changing the width had little effect. Because the normal values were almost totally blocking, the placement of the side boundaries (i.e., the width) would have almost no importance. When we set the side, top, and bottom boundary conditions to be 50 times their normal velocity, we obtain the data in Fig. 7, which is the MTF versus frequency as the width spreading number N_{sx} was varied. The MTF broadens as the width number increases, which corresponds with the actual width becoming smaller because, as the detector narrows, the carriers have less room to wander and blur. This gain in MTF also results in a reduction of the total signal level, as can be seen in Fig. 8. Here is plotted the SiTF of the SPRITE in the same conditions as in Fig. 7. These SiTF numbers are corrected for the changing area of the detector by virtue of the normalization scheme used in the analysis, and so the reductions of signal caused by reductions of area are already compensated. As the width parameter is increased, the overall signal level goes down. The zero-frequency SiTF function is plotted in Fig. 9, and the gradual roll-off of the signal level can be seen distinctly. The conclusions that one can draw is that the width of the detector can be important if the side boundary conditions are leaky, and, if so, increasing the width increases the signal level to a certain point

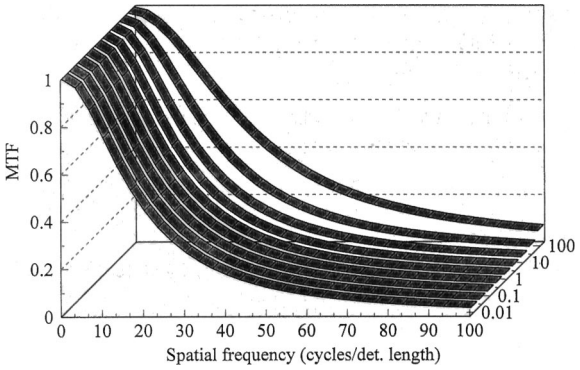

Fig. 7. MTF versus the frequency as the width-spreading parameter is varied from 0.01 to 100 times the normal value. The side boundary conditions are 50 times the normal value.

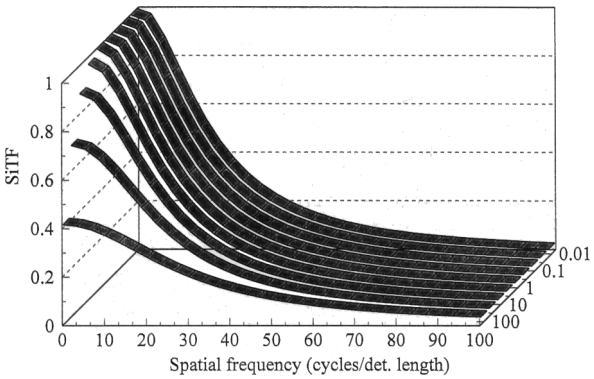

Fig. 8. SiTF versus frequency as the width-spreading parameter is varied from 0.01 to 100 times the normal value. The side boundary conditions are 50 times the normal value.

after which no further gains can be made. In the case of our typical detector, that point was $N_{sx} = 1$.

In Fig. 10 we generated MTF curves for detectors with different contact recombination rates. The velocity was varied over the range of 1/100 to 100 times the nominal value. As expected, the higher the surface velocity, the faster the response. This broadens the MTF curves and indicates that the contact quality affects the MTF. These curves do not address the absolute signal levels, however. A set of

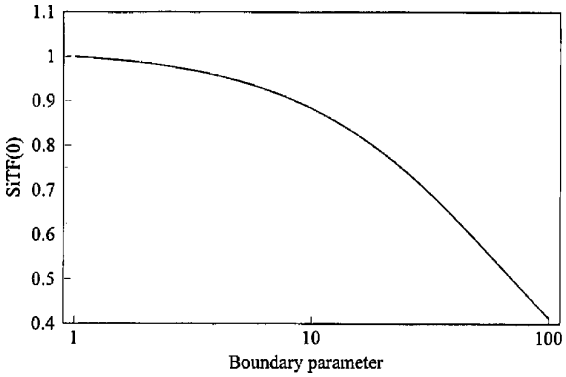

Fig. 9. Variation of the zero-frequency SiTF as the width-spreading parameter is varied from 1 to 100 times the normal value. This corresponds to widths ranging from 1 to 1/10 normal.

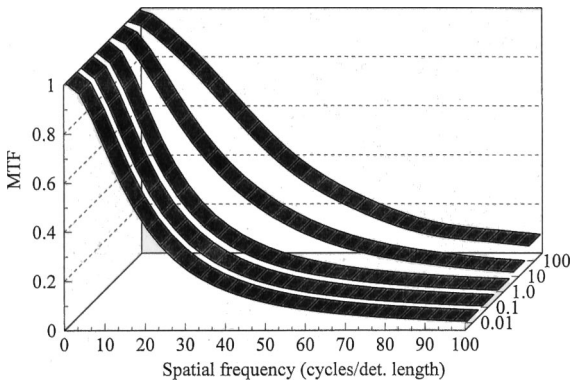

Fig. 10. MTF versus frequency as the contact boundary parameter is varied from 0.01 to 100 times the normal value.

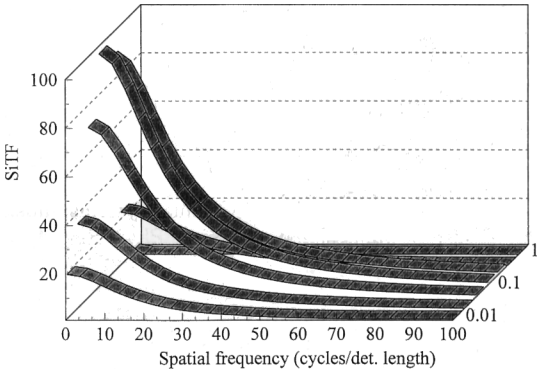

Fig. 11. SiTF versus frequency as the contact boundary parameter is varied from 1 to 0.01.

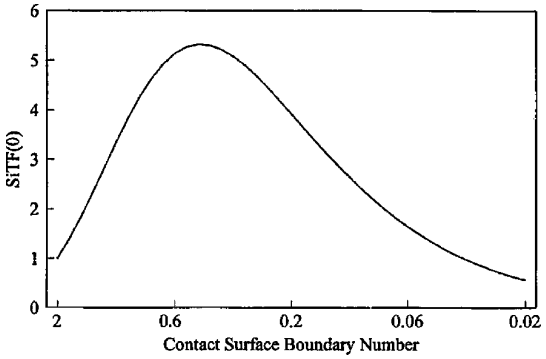

Fig. 13. Zero-frequency SiTF versus the contact boundary parameter. The optimum value of the boundary parameter is around 0.5.

SiTF curves, each normalized by the same normalization constant, is shown in Fig. 11. The boundary number here varies between 1/100 and 1 times the nominal value. These graphs show that for low or high values of contact velocity, the response is reduced. This reduction is so great that it swamps the broadening of the MTF at high surface velocities.

This counterintuitive finding, that better contacts actually produce worse performance, can be explained by looking at the effect of boundary condition on the modes. The two extreme cases of ohmic contacts and blocking contacts are shown in Fig. 12. The figure shows a typical mode profile in the two cases at the readout end of the SPRITE detector with the readout region demarcated. The signal is related to the total charge inside the readout zone, and this is signified by the shaded areas. In the case of ohmic contacts, all the modes of charge distribution have a zero at the end of the detector. This reduces the amount of charge in the readout, as shown by the smaller shaded area. In the case of perfectly blocking contacts, all the modes have their maximum at the end of the detector, which results in a relatively large amount of charge in the readout, as demonstrated by the larger shaded area. This is what causes the increase of signal for partially blocking contacts and the reduction of signal for ohmic contacts.

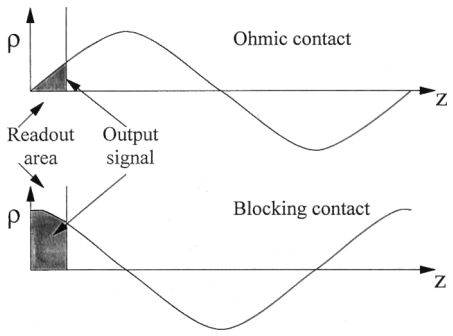

Fig. 12. Diagram of the charge distribution in the SPRITE in ohmic and blocking boundary conditions. The shaded regions represent the readout charge.

Because SiTF performance degrades as the contact conditions become either too high or too low, it stands to reason that an optimum value exists between these two extremes. This optimum can be seen in Fig. 13, where the SiTF at zero frequency is shown as a function of the boundary parameter. This figure clearly illustrates that the signal strength goes through a maximum when the contact boundary parameter is approximately 0.50. This corresponds to a surface recombination velocity, for our typical detector, of 40 cm/s. If possible, such tailoring of the contact velocity of SPRITE detectors could result in large increases in their signal-level performance.

5. Conclusions

In this paper we have presented a new solution to the problem of carrier-transport dynamics in SPRITE detectors through the use of eigenmodal analysis. In doing so, we developed a self-consistent model for the detector. This model and method intrinsically include boundary conditions and full dimensionality and thus are more complete. Through the analysis, certain dimensionless numbers arise that can be used to characterize SPRITE structure parameters and clarify how these parameters affect device performance. Expressions for the MTF have been derived, and various representative computed functions are presented. From these curves, optimum values for the insulating and contact boundary numbers have been determined.

This work was supported by Westinghouse Electric Corporation, Orlando, Fla.

References

1. C. T. Elliot, "Thermal imaging systems," U.S. patent 3,995,159, (30 Nov. 1976).
2. C. T. Elliot, "New detector for thermal imaging systems," Electron. Lett. **17,** 312–313 (1981).
3. D. J. Day and T. J. Shepherd, "Transport in photoconductors—I," Solid State Electron. **25,** 707–712 (1982).

4. T. J. Shepherd and D. J. Day, "Transport in photoconductors—II," Solid State Electron. **25,** 713–718 (1982).
5. G. D. Boreman and A. E. Plogstedt, "Modulation transfer function and number of equivalent elements for SPRITE detectors," Appl. Opt. **27,** 4331–4335 (1988).
6. S. P. Braim and A. P. Campbell, "TED (SPRITE) detector MTF," Inst. Electr. Eng. Conf. **228,** 63–66 (1983).
7. T. Ashley and C. T. Elliot, "Accumulation effects at contacts to *n*-type cadmium mercury telluride photoconductors," Infrared Phys. **22,** 367–376 (1982).
8. M. Boas, *Mathematical Methods in the Physical Sciences* (Wiley, New York, 1983), p. 541.
9. T. Ashley, C. T. Elliott, A. M. White, J. T. M. Wotherspoon, and M. D. Johns, "Optimization of spatial resolution in SPRITE detectors," Infrared Phys. **24,** 25–33 (1984).
10. J. A. Whitlock, G. D. Boreman, H. K. Brown, and A. E. Plogstedt, "Electrical network model for SPRITE detectors," Opt. Eng. **30,** 1784–1787 (1991).
11. S. M. Sze, *Physics of Semiconductor Devices* (Interscience, New York, 1969), p. 71.
12. E. Buckingham, "On physically similar systems; illustrations of the use of dimensional analysis," Phys. Rev. **4,** 345–376 (1914).
13. G. D. Boreman and A. E. Plogstedt, "Spatial filtering by a line-scanned nonrectangular detector: application to SPRITE readout MTF," Appl. Opt. **28,** 1165–1168 (1989).